



Particles II

Access the latest eBook →

11

Advanced
Optical Metrology

Particles II



EVIDENT
OLYMPUS

WILEY

Impact on Biological Systems and the Environment

This eBook is dedicated to the research of Professor David Wertheim.

In collaboration with various groups, Professor Wertheim uses confocal microscopy to analyse the impact of different types of particles on human health and the environment, with a focus on human health-hazardous particles detected with solid-state nuclear track detectors (SSNTD). Download for free, today.

EVIDENT
OLYMPUS

WILEY

Optimized Charge Transport in Molecular Semiconductors by Control of Fluid Dynamics and Crystallization in Meniscus-Guided Coating

Okan Yildiz, Zuyuan Wang, Michal Borkowski, George Fytas, Paul W. M. Blom, Jasper J. Michels,* Wojciech Pisula,* and Tomasz Marszalek*

The effects of the casting speed and solute concentration on the crystallization of 2,7-dioctyl[1]benzothieno[3,2-b][1]benzothiophene (C8-BTBT) during meniscus-guided coating (MGC) are investigated, and three morphological subregimes with increasing casting speed are identified: I) an isotropic domain-like structure; II) unidirectionally aligned crystalline bands; and III) a corrugated dendritic morphology. Interestingly, increasing the solute concentration does not affect these morphologies but merely the associated transition velocities. Numerical simulation of both the fluid dynamics in the coating bead and the crystallization itself not only explains these morphological trends but also the decrease in the width of the crystalline bands of morphology II with the casting speed. They demonstrate that the latter provides an optimal processing window for organic field-effect transistors, with minimized charge trapping, maximized on/off ratio, and reliability factor.

of magnitude and is now higher than those of amorphous silicon devices.^[6] However, it remains challenging to fabricate large-area organic electronics, because defects in the crystalline morphology, such as deformation in the unit cell of the crystal structure,^[7] domain shape distortion, grain boundaries,^[8] and interruption of long-range in- and out-of-plane molecular order,^[9] which may occur at various length scales, critically affect the charge carrier transport, especially in field-effect transistors (FETs). To obtain defect-free thin-films requires a delicate control over the assembly of the OSC molecules during crystallization.

Various solution-based methods have been introduced to control the deposition of the OSC films.^[10] Among them,

1. Introduction

Semi-crystalline organic semiconductors (OSCs) have a proven potential as active layers in electronic thin film applications,^[1] such as transistors,^[2] sensors,^[3] integrated circuits,^[4] and displays.^[5] Over the past decades, the charge carrier mobility in organic field-effect transistors (OFETs) has improved by three to four orders

meniscus-guided coating (MGC) techniques such as dip-coating,^[11] slot-die coating,^[12] solution shearing,^[13] brush coating,^[14] hollow-pen writing,^[15] and zone-casting,^[8,16] emerge as promising candidates, owing to their scalability and potential to optimally control the deposition and crystallization.^[17] In short, these methods rely on a meniscus (or “bead”) of a solution containing the OSC, in contact with a substrate and a dosing head. The substrate translates at a constant speed, while the solvent continuously evaporates. A film is entrained, which, depending on the speed, may be nearly dry or still contain a significant amount of solvent that evaporates after deposition.


Since MGC methods in principle allow for controlling the morphology at different length scales, from macroscopic domain growth^[18] down to long-range molecular ordering,^[19] they are of particular interest to OFETs, which rely on efficient in-plane unidirectional charge transport between the source and drain electrodes. The morphology and surface roughness of the OSC film is directly influenced by the casting speed.^[7,20] However, since the coupling with other parameters, such as the interaction with the solvent, evaporation rate,^[20b,21] concentration,^[22] and substrate surface free energy,^[20c,22,23] is usually strong, attribution of specific morphological features to a single variable is the exception rather than rule.

Despite the plethora of available strategies for the deposition of functional films by MGC, a current understanding on the relation between processing, thin film morphology, and electrical behavior does not suffice to either substantiate the claim of scalability, or allow for the definition of an optimal

O. Yildiz, G. Fytas, P. W. M. Blom, J. J. Michels, W. Pisula, T. Marszalek
Max Planck Institute for Polymer Research
Ackermannweg 10, 55128 Mainz, Germany
E-mail: michels@mpip-mainz.mpg.de; pisula@mpip-mainz.mpg.de;
marszalek@mpip-mainz.mpg.de

Z. Wang
Institute for Measurement and Automation
Division of Sensor Technology and Measurement Systems
Bundeswehr University Munich
Werner Heisenberg Weg 39, 85579 Neubiberg, Germany

M. Borkowski, W. Pisula, T. Marszalek
Department of Molecular Physics
Faculty of Chemistry
Lodz University of Technology
Zeromskiego 116, Lodz 90–924, Poland

 The ORCID identification number(s) for the author(s) of this article can be found under <https://doi.org/10.1002/adfm.202107976>.

© 2021 The Authors. Advanced Functional Materials published by Wiley-VCH GmbH. This is an open access article under the terms of the Creative Commons Attribution License, which permits use, distribution and reproduction in any medium, provided the original work is properly cited.

DOI: 10.1002/adfm.202107976

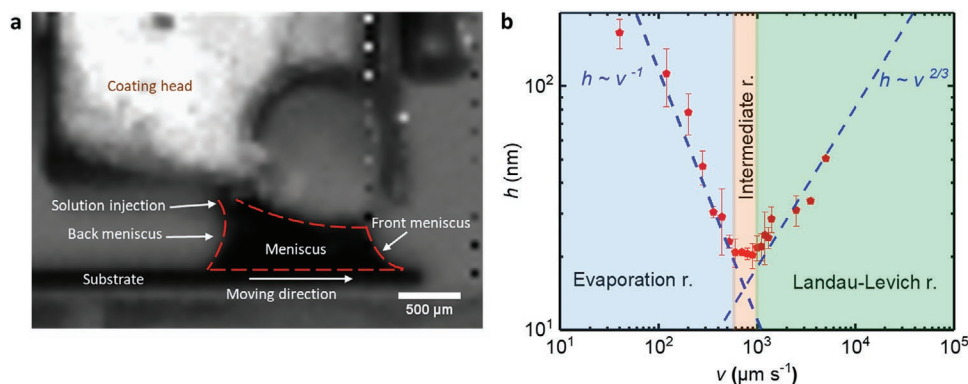


Figure 1. a) Real time image of the zone casting setup and coating bead. The dashed red line shows the outline of the full liquid meniscus. b) Zone cast C8-BTBT film thickness h plotted as a function of the casting speed v . The red dots in (b) represent the experimental data and the dashed blue lines indicate the theoretical scaling extremes for the evaporative ($h \approx v^{-1}$) and Landau–Levich ($h \approx v^{2/3}$) regimes.^[18]

processing window (OPW). For crystallizing OSCs, one generally achieves maximal control at a relatively low casting speed, in the evaporative regime (ER), where crystallization occurs relatively close to the contact line.^[7,20a,b] In this regime, mass transport and structure formation are largely controlled by solvent evaporation. The height of the deposited film scales with the casting speed as: $h \sim v^{-1}$, since the volumetric deposition rate is constant. In the ER, under optimal processing conditions, the unidirectionality of the casting process is expressed in the crystalline morphology. On the other hand, if casting is too fast, a liquid film entrains before significant evaporation occurs and unidirectional control is lost.^[24] In this so-called “Landau–Levich regime” (LLR) the entrainment hydrodynamics determines the film thickness, which scales with the casting speed as: $h \sim v^{2/3}$.^[25] In terms of the OPW, the LLR in effect sets an absolute upper limit for the casting speed. It has been argued that a principle lower limit is given by the retraction velocity of a meniscus of the pure evaporating solvent,^[20b,22] since below this speed an oversupply of solute may lead to crystal nucleation and growth prior to deposition and hence loss of directionality.^[6b,26]

In this combined experimental and modeling study, we demonstrate how the control parameters casting speed and solution concentration affect the definition of the OPW for FET devices based on zone-cast semiconductor films. For the sake of familiarity, we base our investigation on the benchmark molecular semiconductor 2,7-dioctyl[1]benzothieno[3,2-b][1]benzothiophene (C8-BTBT), but expect the generality of our results to carry over to less familiar and novel systems. With increasing casting speed, we identify three morphological subregimes; I) an isotropic domain-like structure; II) a band-like structure following the coating direction; and III) a corrugated morphology lacking directionality. We interpret our experiments using numerical simulations of the steady state fluid dynamics in the bead and the morphology formation in the deposited film, focusing on the onset of the appearance of unidirectionality. The structure formation simulations explain why the bulk solute concentration modulates the onset speed of the aligned subregime, rather than affecting the morphology itself. The second morphological subregime allows for optimized OFET performance. We reveal a direct correlation between the trap density in the OSC film and the casting speed and show how this allows us

to achieve an improved saturation and effective charge carrier mobility, with a high reliability factor.

2. Results and Discussion

Where in our previous work we focused on the combined effect of the casting speed and the evaporation rate,^[18] here we investigate how the speed influences the crystalline morphology of C8-BTBT as a function of the solute concentration. Hereto, zone-casting experiments were performed for v ranging from 40 to 5000 μm s⁻¹ for a constant solution concentration of $c_0 = 1$ mg mL⁻¹ C8-BTBT (molecular structure in Figure S1b, Supporting Information) in tetrahydrofuran (THF). Phenethyl(trichloro)silane (PETS)-modified SiO₂ was used as substrate. It has been argued that an optimum processing temperature T is given for $1 < T_b/T < 1.5$, with T_b the boiling temperature of the solvent ($T_b^{THF} = 66$ °C).^[20b] We used $T = 45$ °C, both for substrate and solution, so that $T_b/T = 1.4$. To elucidate the influence of the concentration, experiments were performed at a constant speed of 440 μm s⁻¹ for $0.25 < c_0 < 8$ mg mL⁻¹. **Figure 1b** shows the dry film thickness as a function of speed for $c_0 = 1.0$ mg mL⁻¹ (see Figure S3, Supporting Information for the thickness profile of the dry films). The dashed lines, indicating the scaling in the ER and LLR, show that our data complies well with the theoretical prediction. Only at very low speed, that is, 40 μm s⁻¹, the experimental thickness of the entrained film is lower than the prediction. In the intermediate regime (I.R.), the film thickness does not depend on v . The resulting films were studied with polarized optical microscopy (POM) and atomic force microscopy (AFM) to characterize the morphology at different length scales (see **Figures 2** and **3**). **Figure 2** displays films obtained at a constant concentration but varying speed, whereas **Figure 3** presents the films cast at different concentration but constant speed.

Irrespective of the concentration, three types of morphologies are observed with the increasing coating speed: I) an isotropic domain-like morphology (**Figures 2a,b** and **3e,f**); II) a “woven” pattern of near-unidirectional crystalline stripes (**Figures 2c–g** and **3a–d**); and III) a corrugated but isotropic structure exhibiting dendritic features (**Figure 2h–j**). Only morphology II bears a structural directionality matching the coating

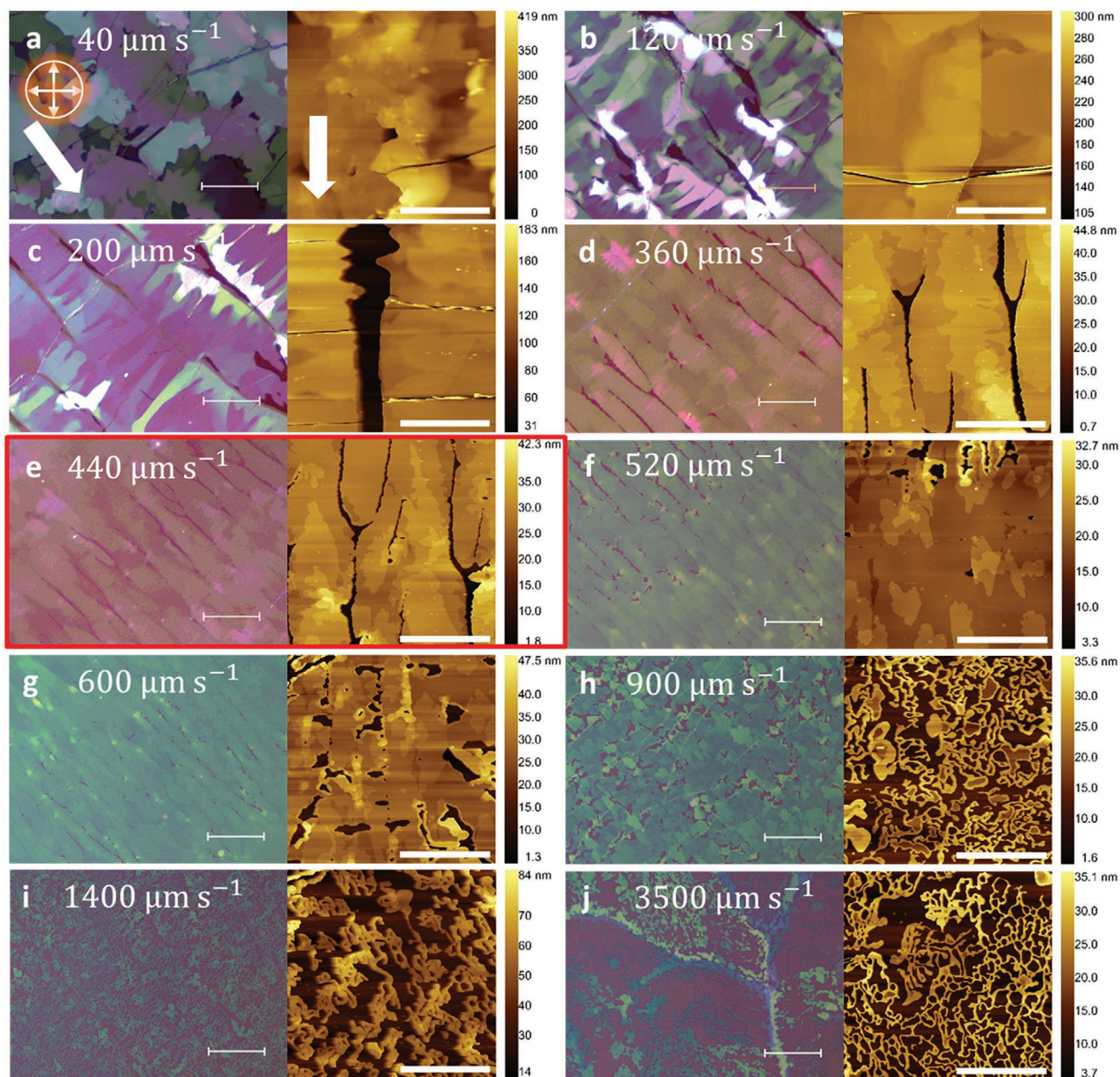


Figure 2. Microscopic analysis (left image: POM [reflection mode], right image: AFM) of zone-cast C8-BTBT films obtained for the coating speeds a) 40, b) 120, c) 200, d) 360, e) 440, f) 520, g) 600, h) 900, i) 1400 and j) 3500 $\mu\text{m s}^{-1}$ at a solute concentration of 1.0 mg ml^{-1} . The scale bars in the POM and AFM images represent 50 and 20 μm , respectively. The white arrows in (a) and (b) indicate the coating direction. Changes in the film obtained for $\nu = 440 \mu\text{m s}^{-1}$ (marked by the red box) as a function of the solute concentration, are presented in Figure 3.

direction. From an application point of view, morphology II is intuitively compatible with unidirectional in-plane charge transport. The loss in directionality by increasing the coating speed, that is, the transition II \rightarrow III, is expected based on the transition from the I.R. to the LLR. In contrast, the loss of directionality by lowering the speed, that is, the transition II \rightarrow I, is somewhat less intuitive but has been observed previously^[20b,27] and ascribed to nucleation and growth occurring in the coating bead, prior to entrainment of the dry film.^[20b,21]

It is interesting to note that a change in the solute concentration does not seem to affect the morphology itself, but merely

the velocities at which the morphological transitions occur. This becomes apparent when comparing Figures 2a–c with Figures 3f,e, and d: the I \leftrightarrow II transition occurs at a higher speed if the solute concentration is increased. Although a primary observation in the present study, it agrees with the work by Janneck et al.,^[27a] who demonstrated that for a fixed coating speed scrambling of the morphology into a non-directional domain-like structure becomes more prominent with increasing concentration. Since such a shift directly affects the eventual processing window, we studied the possible cause of the I \leftrightarrow II transition in more detail. Janneck et al. hypothesized that

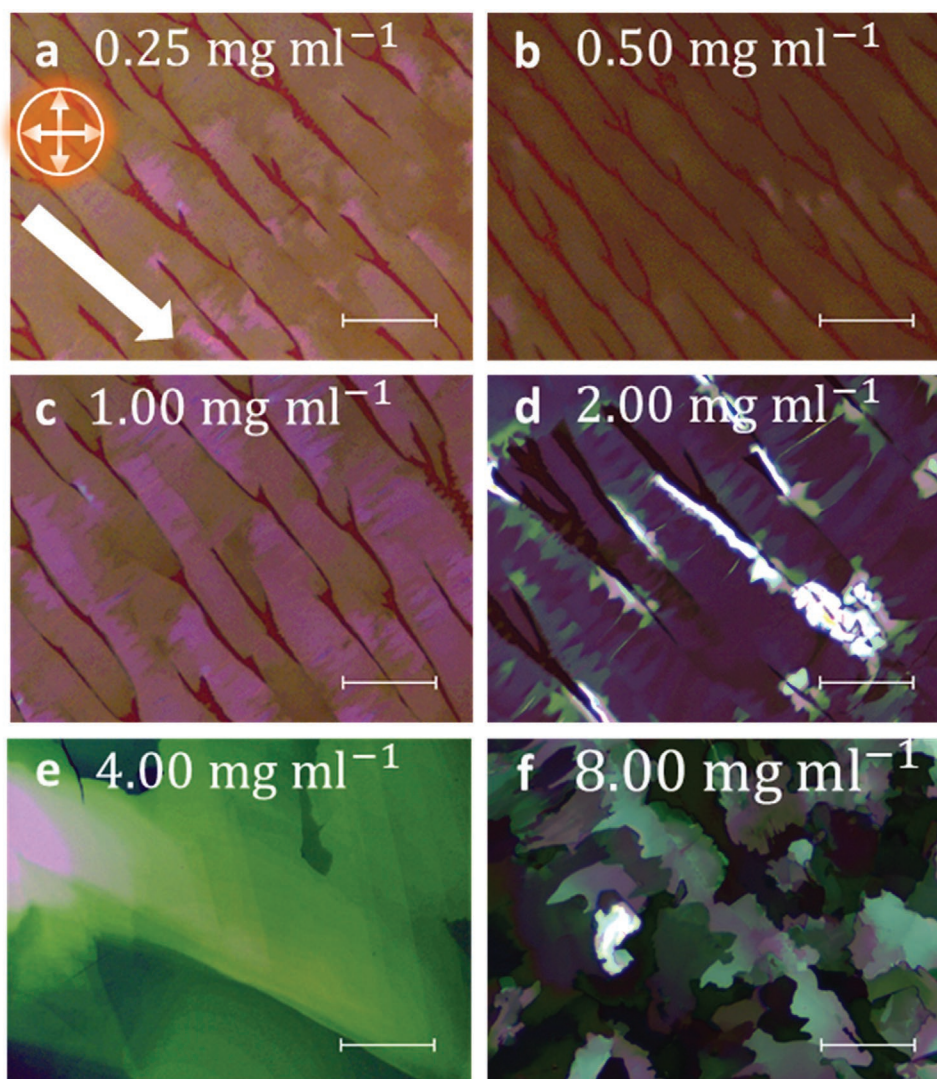


Figure 3. POM images of zone-cast C8-BTBT films obtained at the solute concentrations a) 0.25, b) 0.50, c) 1.00, d) 2.00, e) 4.00 and f) 8.00 mg ml⁻¹. All depositions were performed at a constant casting speed $v = 440 \mu\text{m s}^{-1}$. The white arrows indicate the casting direction. The scale bars are 50 μm .

morphology I results from nucleation in the bead, once the casting speed becomes lower than the retraction velocity of the pure solvent meniscus.^[20b,27a] They reasoned that at such low speeds an oversupply of the solute occurs, as the substrate translation is too slow to absorb sufficient material.^[27a] Upon exceeding supersaturation, random nucleation occurs, giving a non-directional domain structure.

Although a rise in concentration in the bead at low v serves as an explanation for the appearance of morphology I, ascribing its occurrence to a reduced solute absorption by the substrate is unsatisfactory. First, the substrate does not necessarily “absorb” the solute. Instead, the solute rather precipitates or nucleates directly on it. Second, since the outflux of solute is small compared to the evaporative flux, a change in its magnitude is not expected to significantly impact the concentration in the bead. Third, the relation $h \approx v^{-1}$ implies that in the ER the solute outflux is independent of the casting speed. To verify the third point, we perform 2D isothermal

Navier–Stokes (NS) and mass transport simulations in the low speed regime.^[11b,20a,22] The shape of the simulation box (Figure 4a) has been physically predetermined (see Section S1, Supporting Information) and fixed to match the shape of the actual coating bead (Figure 1a). Different from previous simulations,^[20a,22] we cut a small region (see inset Figure 4a) at the tip of the front meniscus to explicitly allow for the solution to exit the simulation domain (outlet region) upon entrainment.^[11b,28] Further details are in the Section S1, Supporting Information.

Figure 4a shows that two vortices appear, resulting from entrainment and backflow of the solution.^[22] The vertical coordinate of the stagnation point at the front meniscus decreases as $y_{\text{stag}} \approx v^{-0.93}$ (Figure 4b), that is, close to the speed-dependence of the simulated film thickness, which agrees excellently with the experimental one for $v > 100 \mu\text{m s}^{-1}$. Indeed, since in the ER the material deposition rate is speed-independent, the relation $h \approx v^{-1}$ can be derived simply by equating the outgoing

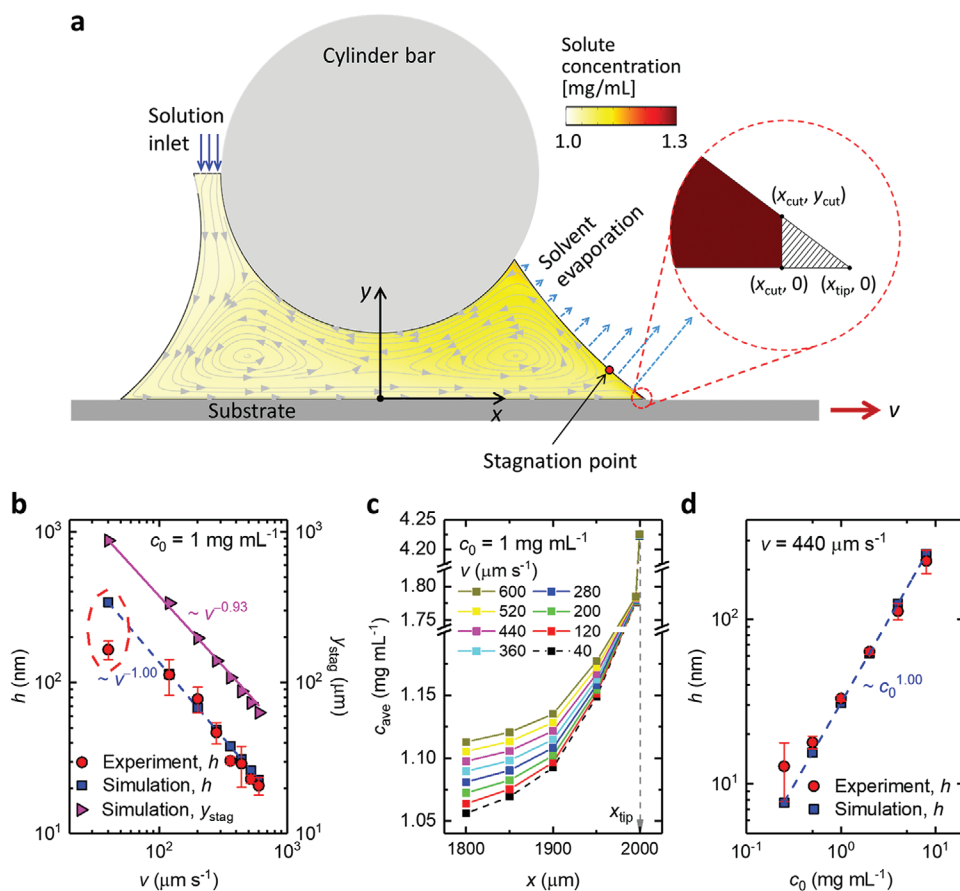


Figure 4. Finite element simulations of the flow and concentration fields in the meniscus during zone-casting of C8-BTBT. a) Illustration of the simulation domain, boundary conditions, and coordinate systems. The shown flow and concentration fields correspond to $y_{\text{gap}} = 500 \mu\text{m}$, $c_0 = 1 \text{ mg mL}^{-1}$, and $v = 440 \mu\text{m s}^{-1}$. b) Film thickness h and the y coordinate of the stagnation point as a function of the substrate speed. The red dashed ellipse shows the discrepancy between the calculation and the experiment at low speed. c) Average solute concentration c_{ave} (averaged in the y direction) near the outlet region (inset of Figure 4a) as a function of x . d) Film thickness as a function of the inlet solute concentration.

fluxes of solvent and solute due to evaporation and deposition to the influx of the native solution.^[29] As a consequence, as long as the ER scaling applies, the concentration far away from the tip remains virtually independent of the casting speed and close to c_0 ,^[29a] as indeed shown by Figure 4c and Figure S2, Supporting Information. Only in the region near the tip the solute concentration rises drastically due to the diverging evaporation rate,^[30] which is independent of v . The linear scaling of the deposited film thickness with the solute concentration $h \approx c_0$ (see Figure 4d) is consistent with the same mass conservation argument.

For $v < 100 \mu\text{m s}^{-1}$, that is, roughly where the II \rightarrow I morphology transition occurs for $c_0 = 1.0 \text{ mg mL}^{-1}$, the simulation overestimates the thickness in comparison to the experimental value (red ellipse in Figure 4b). Such a deviation at very low speed has, for instance, also been observed for MGC of metal-organic frameworks^[31] and phospholipids 30a.^[29a] At the same time, a rise in the simulated concentration in the bead remains absent. This suggests that fixed-domain/fixed meniscus fluid dynamics simulations, such as the present one and used before,^[27a] become inadequate at low v . A possible reason is that a constant volume is trivially not part of the steady state prerequisite. Although a fixed fluid domain is convenient and valid

at an intermediate casting speed sufficiently far away from the LLR, we suspect that it breaks down if v approaches the retraction velocity of the fluid meniscus. Accurate simulation in this regime ideally requires a free liquid/air interface, together with an explicit description of the coexisting phases. However, this makes the calculation highly non-trivial and outside the scope of this study.

Instead, we define a simplified analytical model that captures some essential features of the coating process in an approximate way. We write the mass balances of solute and solvent across the front section of the bead (Figure 5a) as a function of an entrainment flux J_{in} , a reverse flux J_{r} , an evaporative flux J_{ev} , and a deposition rate J_{L} (all in $\text{m}^3 \text{ s}^{-1}$):

$$\bar{\phi} \frac{dV}{dt} + V \frac{d\bar{\phi}}{dt} = J_{\text{in}} \phi_{\text{in}} - J_{\text{r}} \bar{\phi} - J_{\text{L}} \phi_{\text{L}} \quad (1)$$

$$(1 - \bar{\phi}) \frac{dV}{dt} - V \frac{d(1 - \bar{\phi})}{dt} = -J_{\text{ev}} (1 - \bar{\phi}) + J_{\text{in}} (1 - \phi_{\text{in}}) - J_{\text{r}} (1 - \bar{\phi}) - J_{\text{L}} (1 - \phi_{\text{L}}) \quad (2)$$

with $\bar{\phi}$ as the mean volume fraction, V as the volume of the domain, $\phi_{\text{in}} < \bar{\phi}$ as the ingoing concentration, and $\phi_{\text{L}} > \bar{\phi}$ as the concentration in the deposited film. We neglect a dependence

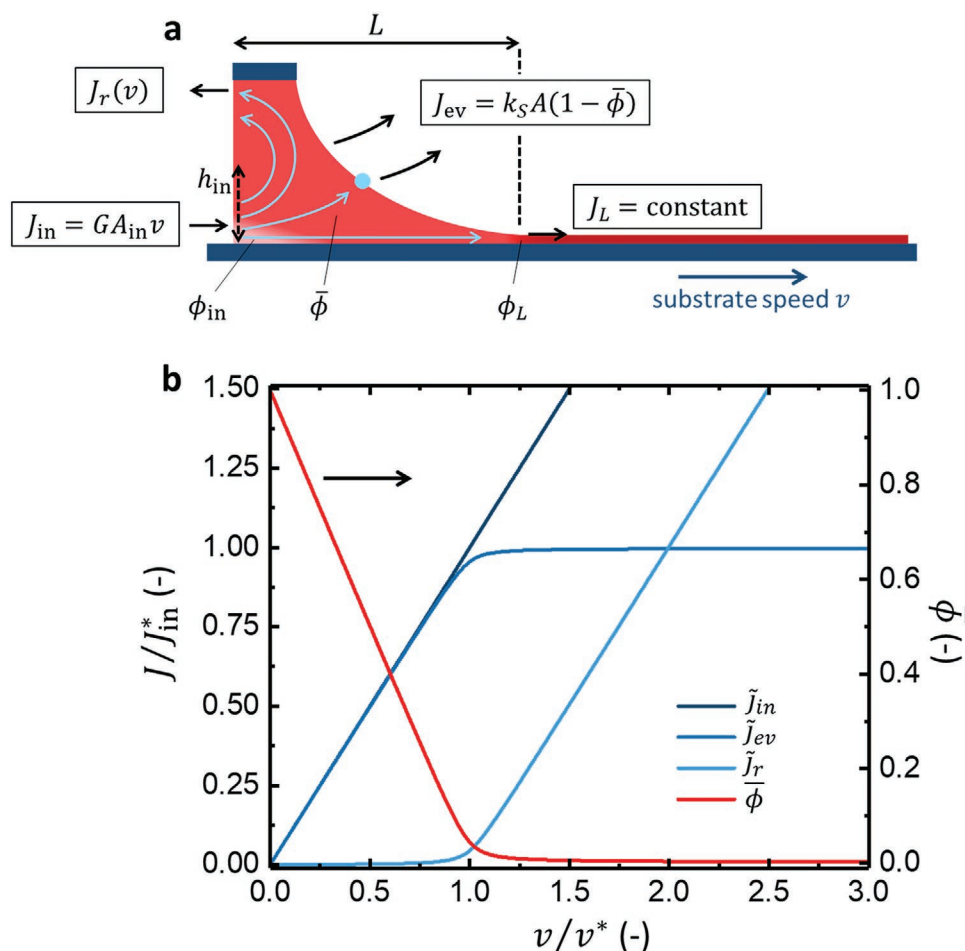


Figure 5. a) Schematic representation of the front part of the coating bead, as assumed by the analytical model for the ER. b) Dimensionless fluxes and mean bead concentration calculated as a function of dimensionless substrate speed, for $c_{in} = 2 \text{ mg mL}^{-1}$ ($\phi_{in} = 0.002$). Tildes in the legend denote dimensionless quantities.

of ϕ_{in} on the casting speed. More importantly, we couple the evaporative flux to the mean bead concentration according to: $J_{ev}(\bar{\phi}) \approx k_s A(1 - \bar{\phi})$, that is, assuming ideal solution conditions. A is the (effective) cross section area of the bead and k_s the retraction velocity of the pure solvent. We furthermore assume a linear relation between J_{in} and v (see Section S2, Supporting Information). The deposition rate J_L is constant in the ER and may be estimated from the experiment. The height of the dry deposited film is: $h = \phi_L J_L / v$.

Solving Equations (1) and (2) for the steady state condition $\frac{dV}{dt} = \frac{d\bar{\phi}}{dt} = 0$ and eliminating J_r as dependent variable, we arrive at an expression for the mean volume fraction:

$$\bar{\phi} = \frac{k_s A - J_{in} + J_L + \sqrt{(k_s A - J_{in} + J_L)^2 - 4k_s A (J_L \phi_L - J_{in} \phi_{in})}}{2k_s A} \quad (3)$$

Next, we define a characteristic casting speed $v^* = 2k_s/G$, for which the entrainment flux equals the evaporative flux of the pure solvent: $J_{in}^* = k_s A$. The prefactor G is a geometric constant, as described in the Section S2, Supporting Information. Substitution gives:

$$\bar{\phi}^* = \frac{J_L + \sqrt{J_L^2 + 4k_s^2 A^2 \phi_0 - 4k_s A J_L \phi_L}}{2k_s A} \quad (4)$$

Since the height of the deposited film is much smaller than the height of the bead, J_L can be ignored, demonstrating the insignificance of solute deposition in determining $\bar{\phi}$. Doing so, we obtain $\bar{\phi}^* \approx \sqrt{\phi_{in}}$.

Figure 5b plots the various fluxes and the mean concentration as a function of the normalized casting speed. Although, due its simplifications, we do not expect the model to produce the exact functional dependence of the fluxes, the trend is consistent with the experimental observations. For $v/v^* > 1$ (high speed), the mean concentration remains close to c_{in} , which is in agreement with the numerical simulations. At the same time, the evaporative flux J_{ev} reaches a near constant value. For $v/v^* < 1$ (low speed) the concentration indeed rises, though not due to a reduced solute absorption by the substrate but rather a decrease in J_r and a longer retention of the solution in the considered volume. The rise in concentration suppresses the solvent activity and hence J_{ev} . This reduction principally prevents (significant) retraction of the meniscus, but the fact that in the experiment the film thickness for $v = 40 \mu\text{m s}^{-1}$ is consistently

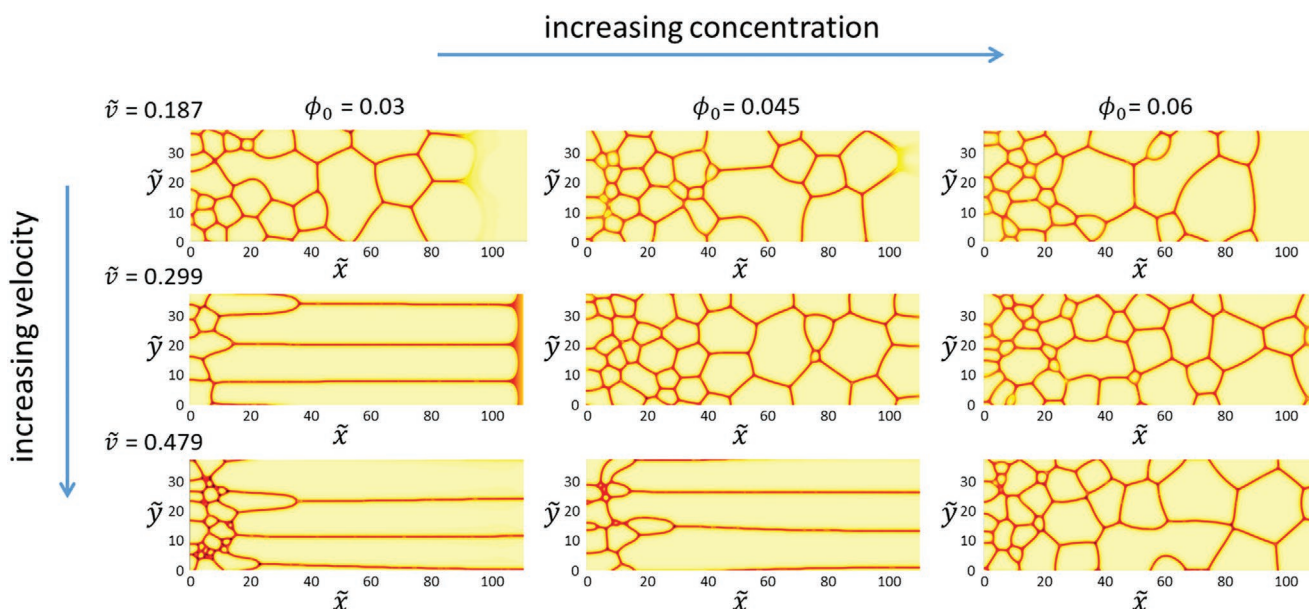


Figure 6. Numerically simulated coated morphologies (crystallinity order parameter, see ref. [18]), plotted as a function of dimensionless space (\tilde{x}, \tilde{y}) for varying native solute volume fraction (ϕ_0) and dimensionless coating velocity $\tilde{\nu}$. For the non-dimensionalization of time and space in these calculations, we refer to ref. [18].

lower than expected (see Figure 4b and note the error bar), testifies a slow retraction, resulting in an effectively higher substrate speed, and hence a lower h . Finally, the increase of the transition speed for morphology I \rightarrow II with c_0 may be explained by a substantial rise in concentration away from the meniscus, as earlier simulations^[27a] have demonstrated.

We find further support for a significantly elevated concentration in the bead at low ν using our recently proposed MGC model.^[18] We recall that this model captures the effect of the speed dependence of the concentration gradient in the tip by interpolating an initial concentration between a high extreme ϕ_{ev} at a low speed and the native concentration ϕ_0 at infinite speed. While in our previous study we fixed ϕ_{ev} below supersaturation, we now consider ϕ_{ev} exceeding it and vary ϕ_0 as in the experiment. Since we only aim for a trend-based comparison, we use a dimensionless speed^[18] and refrain from matching ϕ_0 with the experimental concentrations. **Figure 6** shows that the trend predicted by the model agrees very well with the experiments: a transition from an aligned to a domain-like structure occurs upon lowering the speed. Furthermore, the transition shifts to higher ν upon increasing ϕ_0 .

The speed marking the transition to morphology II is just high enough to prevent supersaturation in the bead, resulting in unidirectional growth parallel to the casting direction (Figure 2c–g).^[18] Morphology II is mostly dense owing to mutual impingement, but also exhibits voids and hence a decreased surface film coverage (**Figure 7a**). Such voids in MGC films of C8-BTBT have been shown to occur periodically or continuously, depending on the casting speed.^[20a,b] A periodicity either reflects a subregime where fluctuating concentration-driven surface tension gradients give rise to long wavelength height undulations^[32] or a stick-slip mechanism due to pinning and depinning of the contact line at the deposit.^[33] **Figure 7a** shows that the RMS roughness of the crystal domains of morphology

II decreases with casting speed, with the smoothest films obtained for $\nu \approx 600 \mu\text{m s}^{-1}$. At the speed range of morphology II, the roughness is in the range of 3.0–6.5 nm, matching the spacing corresponding to one to two interlayers in the C8-BTBT crystal lattice.^[34] Indeed, close inspection (**Figure S6**, Supporting Information) reveals a terrace-like structure with a step height of 2.9 nm, exactly matching the lattice spacing. The unidirectional crystal growth and the low RMS roughness makes morphology II a suitable candidate for implementation in OFET devices.

Figure 7b reveals a near linear decrease in the mean width \bar{w} of the stretched domains with increasing coating velocity. A possible cause for the decrease in \bar{w} with increasing substrate velocity (**Figure 2b–g**) is a decrease in the time available for Ostwald ripening. During this process large (sub)domains grow at the expense of small ones on account of a concentration gradient arising from a difference in curvature. Since during ripening the mean domain size increases with time as $\propto t^{1/3}$, the ER should yield an approximate dependence of $\bar{w} \propto \nu^{-1/3}$. However, the fact that the speed dependence of \bar{w} is steeper (**Figure 7b**) indicates the presence of a contributing mechanism. To understand this, we note that small domains principally testify a high nucleation density, providing an “early stage argument” based on the notion that a continuous solvent quench occurs in the foot of the meniscus where the viscous forces roughly balance the surface tension. As in the ER the height of the film entrained from the gradient in the tip of the meniscus decreases with increasing speed, an increase in the latter results in a deeper quench and hence an increased nucleation density.^[18]

We demonstrate this by numerical simulation (**Figure 7c**) of a section of the film in which evaporation induces the formation of new nuclei on the left side of the domain during slow (top panels) and faster coating (bottom panels). Successful nucleation is clearly more frequent if substrate translation is fast,

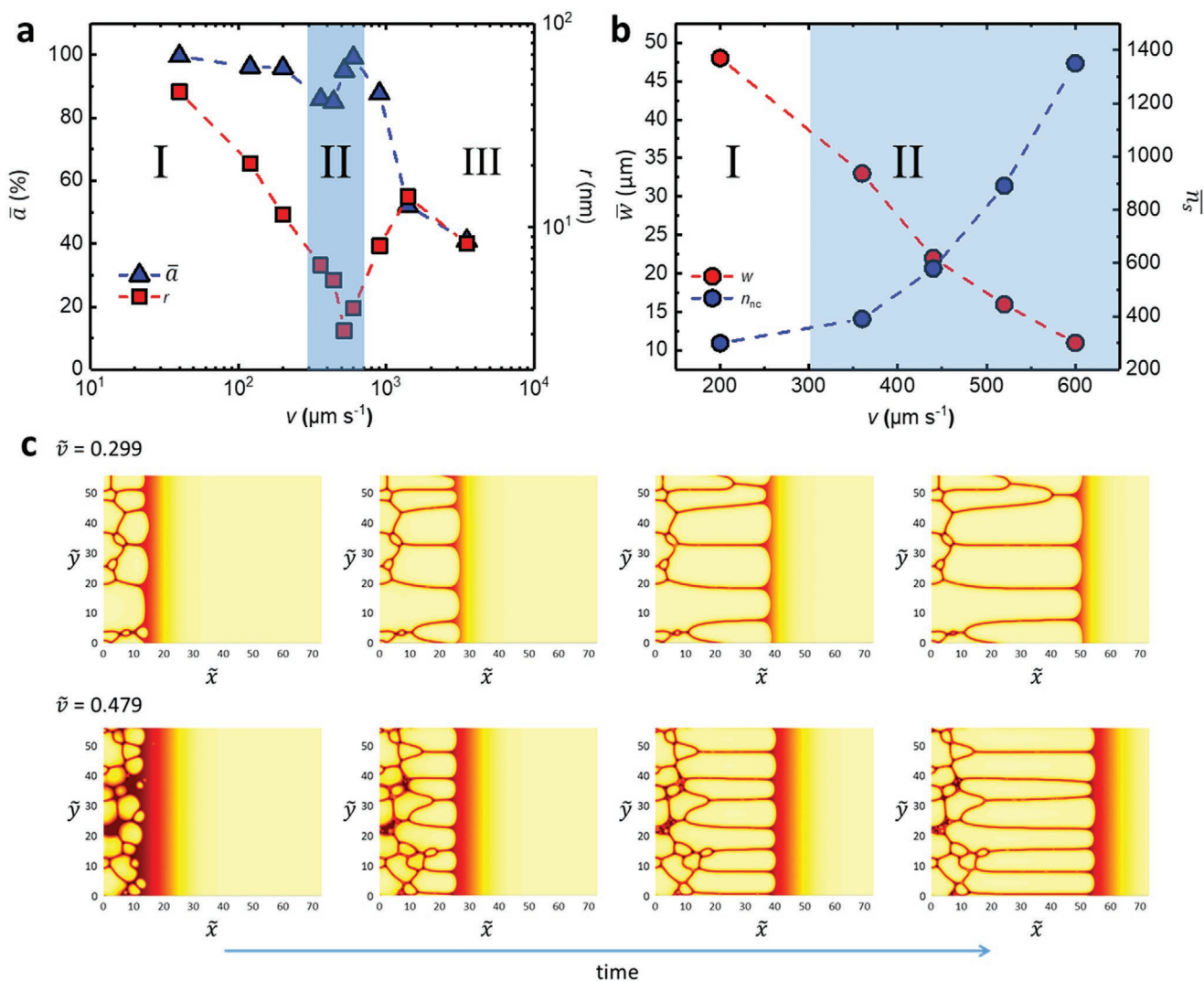


Figure 7. Quantitative analysis of the films displayed in Figure 2. a) Film coverage (\bar{a}) and RMS roughness r of the C8-BTBT films plotted as a function of casting speed ν . The morphological subregimes are indicated with roman numbers. b) Mean crystal domain width (\bar{w}) and mean number of stripes (\bar{n}_s) encountered in morphology II perpendicular to the coating direction. \bar{n}_s has been obtained using the relation: $\bar{n}_s = \bar{w}a/W$, with W the width of the meniscus. Dashed-lines in (a) and (b) are eye guides. c) Numerical simulation of aligned crystallization (morphology II) during MGC. Substrate translation occurs from right to left. The images show the crystallinity, as well as the normalized height (see ref. [18] for details) as a function of dimensionless space (\tilde{x}, \tilde{y}) for two different dimensionless casting speeds (see figure) and $\phi_0 = 0.03$. For the non-dimensionalization of time and space in these calculations, we refer to ref. [18].

resulting in narrower domains as also experimentally observed. For $c_0 = 1.0 \text{ mg mL}^{-1}$, this form of nucleation and growth persists up to approximately $600 \mu\text{m s}^{-1}$. Beyond this speed, a second morphological transition occurs towards a corrugated but isotropic structure (Morphology III). Concomitantly, the film coverage decreases abruptly, whereas the roughness follows the opposite trend (Figure 7a). Although Morphology III (Figure 2h–j) has dendritic features, it is not outspokenly “tree-like” as observed before for C8-BTBT,^[11b] as well as other molecular semiconductors applied by MGC.^[6d,35]

As expected for the LLR, Morphology III does not express the directionality of the coating process. Hence, its features are isotropic although the lateral distribution of solid material is not homogeneous. In fact, Morphology III may have resulted, at least partially, from dewetting instabilities interfering with

drying and crystallization. In particular Figure 2j bears a striking resemblance with structures formed by such instabilities in drying films of colloidal suspensions.^[36] The occurrence of dewetting instabilities is perhaps not surprising, considering the fact that for both a drying suspension and a solution of a low molecular weight semiconductor the viscosity remains relatively low and therefore less capable of counteracting flow induced by capillary forces.

Although in this work we use one single processing temperature, we provide some discussion on the effects on the film characteristics and crystalline regimes due to temperature variation. A change in temperature usually affects a plurality of parameters, most prominently the evaporation rate, diffusivity, viscosity, and solvation. In the present case the impact of a change in temperature on the evaporation rate is most likely

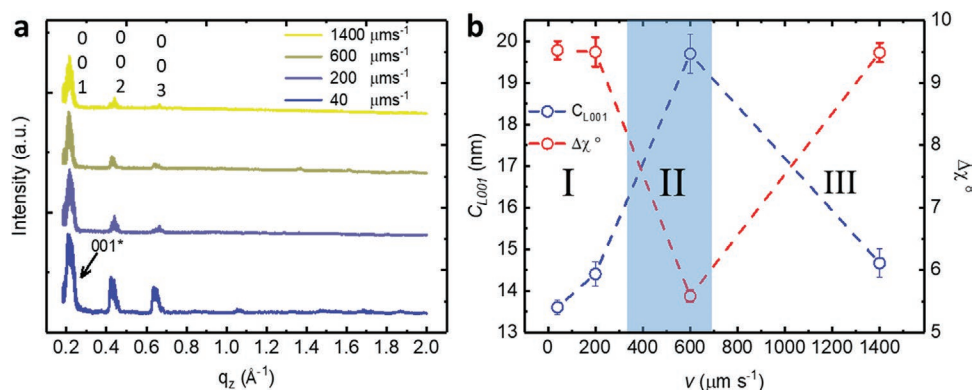


Figure 8. a) Out-of-plane profiles of GIWAXS patterns for C8-BTBT films zone-cast at different coating speeds. b) Coherence length of the 001 reflection in interlayer direction and $\Delta\chi$ as a function of casting speed. The three morphological regimes are indicated in the graph. Dashed lines are eye guides.

a dominant factor, the solution viscosity being already low and the non-polar molecular interaction depending only weakly on temperature (typically $\propto 1/T$). As we have shown before, an increased evaporation rate gives a thicker film in the ER, whereas in the LLR (hydrodynamic) regime the film thickness is not impacted.^[18] For this reason, the IR will shift to a higher coating speed with increasing temperature. A higher temperature also causes a steeper rise in the concentration and hence an elevated nucleation density,^[18] hence suppressing the structure size in the crystalline film, that is, stripe width in case of an aligned morphology. This applies especially to Morphology II and III, which form close to or downstream from the contact line. As for Morphology I, the influence of the temperature is probably smaller, as nucleation takes place inside the bead while the solution is replenished. We furthermore argue that an increase in the evaporation rate causes the transition velocity from Morphology I to II to shift to a higher value, just as observed above for an increase in the bulk concentration.

To gain further structural information on the deposited C8-BTBT thin films including the π -stacking and interlayer distances, long-range crystalline order, grain size and molecule's orientation relative to the substrate, grazing incidence wide-angle X-ray scattering (GIWAXS) was employed. It is generally believed that any variation in the molecular arrangement concerning unit cell dimension,^[13b] long range order and "edge-on" or "face-on" packing motif significantly influence on the charge carrier transport. The analysis of the GIWAXS data is presented in **Figure 8**. Figure 8a presents 1D out-of-plane integration profiles of GIWAXS patterns (Figure S7, Supporting Information) obtained for zone-cast C8-BTBT at varying speed. The interlayer distance of 2.91 nm for all samples is determined from the main reflection observed at $q_z = 0.216 \text{ \AA}^{-1}$ and $q_{xy} = 0 \text{ \AA}^{-1}$ (Figure 8a and Figure S8, Supporting Information). Higher order reflections (up to 3rd) imply long-range organization of the molecules in the out-of-plane direction of the film. This interlayer distance is in agreement with the length of a molecule, as presented in the literature^[37] and suggests that the long axis of the C8-BTBT molecule is arranged perpendicular to the substrate surface.

In this edge-on organization, π -stacking direction is arranged parallel to the surface which is beneficial for in-plane charge transport. The crystal lattice of the molecules in thin films is

in agreement with single crystal data.^[26a,b] Detailed analysis of the reflection assigned to the interlayer distance shows that for 40 $\mu\text{m s}^{-1}$ substrate speed an additional a 001* reflection appears at $q_z = 0.210 \text{ \AA}^{-1}$, corresponding to a d-spacing of 2.71 nm (Figure 8a). This is due to a different molecular tilting on the substrate induced by the PETS self-assembled monolayer (SAM), as well as the vertical temperature gradient across the film (see Experimental Section). A longer crystallization time and interactions between the alkyl side chains can enhance molecular packing of C8-BTBT molecules in the out-of-plane direction.^[38] Comparable results, that is, a decrease in the interlayer distance, has been observed for C8-BTBT blended with poly(4-styrene sulfonic acid) (PSS).^[37]

The role of the substrate speed on the molecular order (tilting angle) can be first observed by variation in the orientation and domain size in the out-of-plane direction. As evident from Figure 8b, the coherence length C_{L001} , calculated on the basis of FWHM value of the 001 peak, increases with higher v in the ER. The highest C_{L001} is observed for 600 $\mu\text{m s}^{-1}$ which corresponds to a h of 20 nm, suggesting a homogenous molecular organization throughout the height of the layer. The lower C_{L001} values at lower speeds in the ER and in the entire LLR (morphologies I and III indicated in Figure 8b) suggest a higher disorder of the C8-BTBT molecules. This is confirmed by the domain misalignment presented by the angular intensity distribution of the 001 reflection in the GIWAXS patterns. For samples deposited at $v < 360 \mu\text{m s}^{-1}$ (morphology I) and $v > 900 \mu\text{m s}^{-1}$ (morphology III) the FWHM is found equal to 9.5° . An almost twice lower value is observed for the speed range of $360 \mu\text{m s}^{-1} < v < 900 \mu\text{m s}^{-1}$, confirming the highest degree of molecular order of the thin film cast at 600 $\mu\text{m s}^{-1}$.

Finally, we consider the influence of the casting speed on the π -stacking distance (Figure S8, Supporting Information, 020 reflection). For a relatively low casting speed of 200 $\mu\text{m s}^{-1}$, at which the shearing forces induce unidirectional molecular ordering, the π -stacking distance is 3.35 \AA . By applying a higher casting speed of 600 $\mu\text{m s}^{-1}$, the π -stacking distance is reduced to 3.25 \AA . This is probably connected with a compressively strained molecular lattice of the C8-BTBT, previously proven for solution sheared TIPS-pentacene^[13b] and C8-BTBT:PSS blend.^[37] For the casting speeds of 40 and 1400 $\mu\text{m s}^{-1}$, we observed two peaks which can be assigned to π -stacking distance of 3.25 and 3.33 \AA .

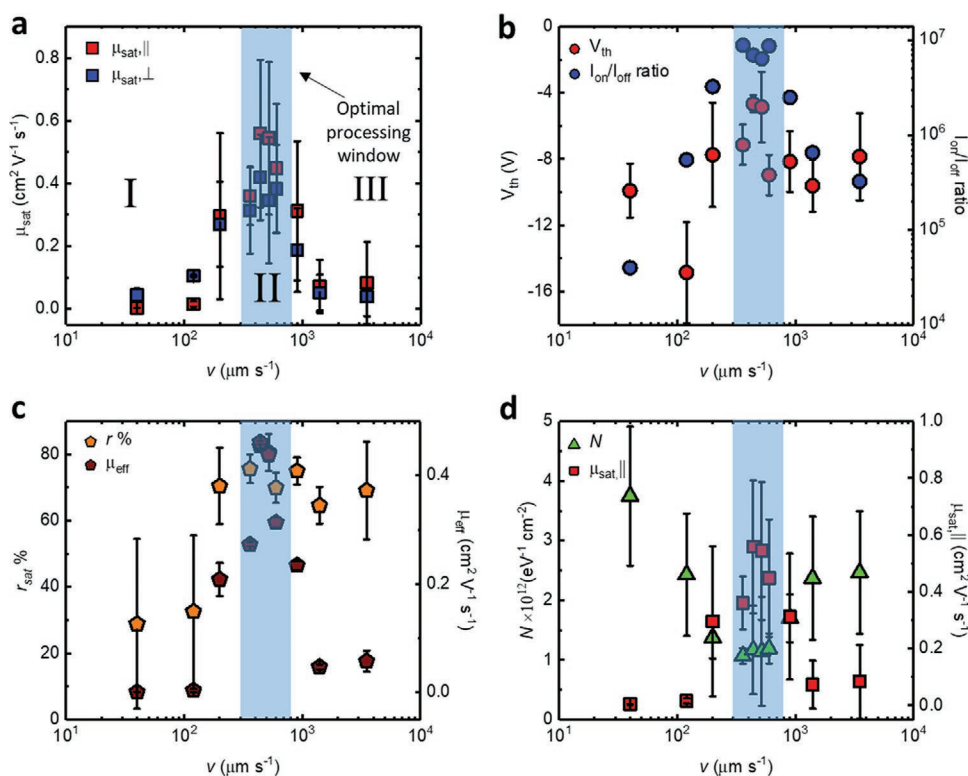


Figure 9. OFET performance as a function of ν with a) saturation charge carrier mobility μ_{sat} , b) threshold voltage V_{th} and $I_{\text{on}}/I_{\text{off}}$ ratio, c) reliability factor r_{sat} and effective mobility μ_{eff} , and d) trap density N and μ_{eff} . Morphology regimes I, II, and III are indicated in the graph (a) together with the optimal processing window.

Due to the low intensity of π -stacking reflection (020), we were not able to determine the in-plane coherence length.

The charge carrier transport in the zone-cast films is investigated in field-effect transistors with a bottom-gate, top-contact (BGTC) configuration. A MoO_3/Ag bilayer was used as top contact to reduce the charge injection barrier between the work function of the metal and the HOMO level of the semiconductor.^[39] The analyses were done over 15 devices for each case.

The isotropic domain-like morphology I (obtained for $\nu = 40 \mu\text{m s}^{-1}$) leads to poor charge carrier transport, as evidenced by a low saturation mobility μ_{sat} of approximately $10^{-3} \text{ cm}^2 \text{ V}^{-1} \text{ s}^{-1}$, both parallel (\parallel) and perpendicular (\perp) to the casting direction (Figure 9a and Figure S9a, Supporting Information). Such a low charge carrier mobility is explained by a high density of grain boundaries, as confirmed by the AFM images presented in Figure 2a,b. This type of morphology results in the highest average threshold voltage of $V_{\text{th}} = -10 \pm 2 \text{ V}$ (Figure 9b). The polycrystalline domains are stretched for $\nu = 120 \mu\text{m s}^{-1}$ that induces a one order of magnitude increase in the charge carrier mobility to approximately $10^{-2} \text{ cm}^2 \text{ V}^{-1} \text{ s}^{-1}$. The value remains still low due to the formation of morphology I. A significant mobility increase by two orders of magnitude to $\mu_{\text{sat},\parallel} = 0.30 \text{ cm}^2 \text{ V}^{-1} \text{ s}^{-1}$ is observed at the morphology I \rightarrow II transition for $\nu = 200 \mu\text{m s}^{-1}$ (Figure 9a). Figure 9b shows that at the I \rightarrow II transition the overall device performance improves with a threshold voltage decreasing by a factor of three and the $I_{\text{on}}/I_{\text{off}}$ ratio increasing by two orders of magnitude. The morphology I \rightarrow II transition provides an improved electrical performance not only due to the

lower density of the grain boundaries but also due to the change in the contact resistance R_{con} at the electrode/semiconductor interface and the bulk resistance R_{bul} in the semiconductor. The resistance profile of the BGTC device configuration is shown in Figure S11a, Supporting Information. We calculated $R_{\text{con}} + R_{\text{bul}}$ by using transfer-length method (TLM)^[40] for $\nu = 200 \mu\text{m s}^{-1}$ (Figure S11b, Supporting Information) and $520 \mu\text{m s}^{-1}$ (Figure S11c, Supporting Information). The $R_{\text{con}} + R_{\text{bul}}$ was found to be $1.10 \times 10^5 \Omega \text{ cm}$ for $200 \mu\text{m s}^{-1}$ and $0.10 \times 10^5 \Omega \text{ cm}$ for $520 \mu\text{m s}^{-1}$. The calculated difference originates from the film thickness where thicker film increases R_{bul} . More details for electrical output and transfer characteristics of the OFETs are presented in Section S3, Supporting Information.

For $\nu > 900 \mu\text{m s}^{-1}$, with the drop of the molecular alignment at the morphological transition II \rightarrow III, the charge carrier mobility decreases to $\mu_{\text{sat},\parallel} = 0.30$ and $\mu_{\text{sat},\perp} = 0.18 \text{ cm}^2 \text{ V}^{-1} \text{ s}^{-1}$. A more drastic decrease in the charge carrier mobility down to the order approximately $10^{-2} \text{ cm}^2 \text{ V}^{-1} \text{ s}^{-1}$ is seen for higher coating speeds of 1400 and $3500 \mu\text{m s}^{-1}$ which is attributable to the higher disorder, as evidenced by a low coherence length and misalignment of molecules (Figure 8b). The threshold voltage and $I_{\text{on}}/I_{\text{off}}$ ratio for morphology III are comparable to those of morphology I (Figure 9b), showing that the speed range associated with morphology II provides the OPW for the charge carrier transport in OFETs. Since the film coverage is variable in respect to casting speed (Figure 7a), we calculated true $\mu_{\text{sat},\parallel}$ by multiplying the film coverage with the channel width. However, the obtained trend remained the same (Figure S12, Supporting Information) as it is shown in Figure 9a.

C8-BTBT does not exhibit any charge carrier transport anisotropy due to its molecular arrangement in the crystal lattice.^[41] We ascribe the difference between the values measured parallel and perpendicular to the casting direction to the voids in the film, as well as the reduction in the crystal width, as shown in Figure 7b. In Figure 9a, this speed range of morphology II also showed the highest average charge carrier mobility of $0.36 \leq \mu_{\text{sat},\parallel} \leq 0.56 \text{ cm}^2 \text{ V}^{-1} \text{ s}^{-1}$ and $0.31 \leq \mu_{\text{sat},\perp} \leq 0.42 \text{ cm}^2 \text{ V}^{-1} \text{ s}^{-1}$. The crystalline stripes in morphology II likely exhibit long-range molecular order, which explains its favorability for in-plane charge carrier transport. Admittedly, μ_{sat} is found relatively moderate for the zone-cast C8-BTBT films in comparison to previously published reports.^[20c,b] On the other hand, the devices morphology II with show a high reliability factor (r_{sat}) of $\geq 65\%$ and effective mobility (μ_{eff}) (Figure 9c). A more detailed explanation is given in the Supporting Information, Section 3 and ref. [42].

We establish an additional link between charge carrier transport and morphology by calculating the density of interfacial and bulk deep traps using the subthreshold swing SS , defined as:^[43]

$$SS = \frac{k_B T \ln 10}{q} \left[1 + \frac{q^2}{C_i} N \right] \quad (5)$$

with k_B the Boltzmann constant, T the absolute temperature, q the elementary charge, N the trap density, and C_i the insulator capacitance. As shown in Figure 9d, N gradually decreases in the ER. and levels off at a minimum plateau in the OPW of $\approx 1 \times 10^{12} \text{ eV}^{-1} \text{ cm}^{-2}$ for the speed range of $360 \leq v \leq 600 \text{ } \mu\text{m s}^{-1}$, that is, for morphology II. As expected, N increases again to approximately $2.5 \times 10^{12} \text{ eV}^{-1} \text{ cm}^{-2}$ between 600 and $3500 \text{ } \mu\text{m s}^{-1}$, that is, for morphology III. Similarly, trap density of single-crystal pentacene was found equal to $1 \times 10^{12} \text{ eV}^{-1} \text{ cm}^{-2}$.^[43] The defined window is consistent with the morphology analyses in which morphology II ($360 \text{ } \mu\text{m s}^{-1} \leq v \leq 600 \text{ } \mu\text{m s}^{-1}$) represents the OPW. In summary, r_{sat} reaches the highest values for morphology II due to linear $I_{\text{ds}}^{1/2}$ (ideal) transfer curves, V_{th} closer to 0 V as well as reduced value of N . For this reason, we do not only evaluate μ_{sat} but also r_{sat} and N to understand the non-ideality of transfer curves. We agree with the procedure proposed in literature in ref. [43] which is that r_{sat} and μ_{eff} should be compared in order to understand and compare non-ideal/ideal behavior of organic transistors.

3. Conclusion

In conclusion, the morphology of zone-cast thin films of the molecular semiconductor C8-BTBT can be categorized into three subregimes, featuring crystalline domains that are: I) isotropic; II) unidirectional crystal stripes; and III) corrugated and dendritic. Whereas (I) and (II) are typically found in the evaporative coating regime, (III) is primarily produced in the Landau–Levich regime. Increasing the solution concentration does not directly affect the morphology, but merely increases the critical casting speeds that mark the transitions between the morphology subregimes. Numerical simulation of the fluid dynamics in the coating bead and crystallization in the deposited film, explains the occurrence of morphology I by premature

random nucleation resulting from a significantly elevated local solute concentration at low speed. The band-like structure, low roughness and, as shown by GIWAXS, significant molecular order obtained in subregime II, provides for optimal electrical performance in organic field-effect transistors. We expect the insight gained in this work, in particular the proposition of an OPW, to be valuable for ensuring reproducible device manufacture by meniscus-guided coating techniques.

4. Experimental Section

Materials and Substrate Preparation: Highly doped silicon substrates with a 300 nm thick SiO_2 layer were cleaned in an ultrasonic bath by using acetone, hexane, toluene, and isopropyl alcohol. After exposure to oxygen plasma for 10 min, the surface was treated with trichloro(phenethyl)silane (PETS) in a vacuum oven heated at $140 \text{ }^\circ\text{C}$ and vacuumed to 10 mbar for 3 h. All solvents, C8-BTBT, and PETS were purchased from Sigma-Aldrich and used as received.

Zone-Casting: Zone-casting was performed in a specially designed setup which is depicted in Figure 1. The height distance between the teflon blade and the substrate was fixed to 0.50 mm. The solution and the substrate were heated at $45 \text{ }^\circ\text{C}$. The substrate speed was controlled in the range from 40 to $5000 \text{ } \mu\text{m s}^{-1}$.

Morphological and Structural Characterization: Film thickness measurements were done by a KLA Tencor Profilometer. Optical Microscopy Images were obtained by a Leica Light Microscope in reflected light. AFM studies were done using Park System NX-20 in tapping mode. GIWAXS measurements were performed at the Dortmund Electron Accelerator (DELTA) Synchrotron Facility (Dortmund, Germany), beamline BL09. The photon energy was set to 10 keV ($\lambda = 1.24 \text{ \AA}$). The sample chamber was vacuumed to $\approx 1 \text{ m bar}$ during the measurement. The incident angle (α_i) of the X-ray beam was adjusted individually for each sample in the range of $0.08\text{--}0.12^\circ$. The scattered intensity was recorded by a 2D image plate (MAR345, marXperts GmbH, Norderstedt, Germany). The exposure time was 180 s. The q -range ($q = 4 \times \pi \times \sin \theta \times \lambda^{-1}$) was calibrated using silver behenate standard. The data was processed and analyzed using Datasqueeze (University of Pennsylvania, Philadelphia, PA, USA) and OriginPro (OriginLab Corporation, Northampton, MA, USA).

Transistor Fabrication and Characterization: BGTC device configuration was used for the OFETs. C8-BTBT was dissolved in THF with the concentration of 1 mg mL^{-1} . After zone-casting the active layer, 10 nm thick MoO_3 was thermally evaporated on top of the film through a shadow mask with the evaporation rate of 0.2 \AA s^{-1} followed by 50 nm thick Ag at the evaporation rate of 1 \AA s^{-1} . The channel length of the electrode geometry was ranging from 30 to $80 \text{ } \mu\text{m}$, and the width of the electrodes was $1000 \text{ } \mu\text{m}$. Afterwards, the devices were annealed at $60 \text{ }^\circ\text{C}$ for 12 h in a N_2 -filled glove box. Electrical characterizations were done using Keithley 4200-SCS in a N_2 -filled glove box. Field-effect mobilities were calculated in the saturation regime using conventional transconductance analysis given by $\mu_{\text{FET}} = (2L/W)(1/C_i)(\partial\sqrt{I_{\text{D}}}/\partial V_{\text{G}})^2$. Measurements were done for V_{gs} sweeping from 10 to -40 V at a constant $V_{\text{ds}} = -40 \text{ V}$.

Supporting Information

Supporting Information is available from the Wiley Online Library or from the author.

Acknowledgements

O.Y. acknowledges the financial and technical support from Max Planck Institute for Polymer Research. O.Y. and T.M. acknowledge Dortmund

Electron Accelerator (DELTA) for grazing-incidence wide-angle X-ray scattering (GIWAXS) measurements. M.B. and T.M. acknowledge the Foundation for Polish Science financed by the European Union under the European Regional Development Fund (POIR.04.04.00-00-3ED8/17-01). W.P. acknowledges the National Science Centre, Poland, through the grants UMO-2015/18/E/ST3/00322 and UMO-2019/33/B/ST3/1550. Z.W. and G.F. acknowledge the financial support by ERC AdG SmartPhon (Grant No. 694977). Open Access funding provided by the Max Planck Society. Open access funding enabled and organized by Projekt DEAL.

Conflict of Interest

The authors declare no conflict of interest.

Data Availability Statement

The data that support the findings of this study are available from the corresponding author upon reasonable request.

Keywords

charge carrier transport, field-effect transistors, organic semiconductors, solution deposition, thin film morphology

Received: August 11, 2021

Revised: September 20, 2021

Published online: October 7, 2021

- [1] M. Kastler, W. Pisula, F. Laquai, A. Kumar, R. J. Davies, S. Balushev, M. C. Garcia-Gutiérrez, D. Wasserfallen, H. J. Butt, C. Riekel, G. Wegner, K. Müllen, *Adv. Mater.* **2006**, *18*, 2255.
- [2] H. Kleemann, K. Krechan, A. Fischer, K. Leo, *Adv. Funct. Mater.* **2020**, *30*, 1907113.
- [3] L. Torsi, M. Magliulo, K. Manoli, G. Palazzo, *Chem. Soc. Rev.* **2013**, *42*, 8612.
- [4] S. Yuvaraja, S. G. Surya, M. T. Vijjapu, V. Chernikova, O. Shekhah, M. Eddaoudi, K. N. Salama, *Phys. Status Solidi RRL* **2020**, *14*, 2000086.
- [5] M. Mizukami, S. Oku, S.-I. Cho, M. Tatetsu, M. Abiko, M. Mamada, T. Sakanoue, Y. Suzuri, J. Kido, S. Tokito, *IEEE Electron Device Lett.* **2015**, *36*, 841.
- [6] a) H. Sirringhaus, *Adv. Mater.* **2014**, *26*, 1319; b) S. Kwon, J. J. Kim, G. Kim, K. Yu, Y. R. Jo, B. J. Kim, J. J. Kim, H. Kang, B. Park, K. Lee, *Adv. Mater.* **2015**, *27*, 6870; c) H. Minemawari, T. Yamada, H. Matsui, J. Tsutsumi, S. Haas, R. Chiba, R. Kumai, T. Hasegawa, *Nature* **2011**, *475*, 364; d) Y. Diao, B. C. Tee, G. Giri, J. Xu, D. H. Kim, H. A. Becerril, R. M. Stoltenberg, T. H. Lee, G. Xue, S. C. Mannsfeld, Z. Bao, *Nat. Mater.* **2013**, *12*, 665.
- [7] G. Giri, E. Verploegen, S. C. B. Mannsfeld, S. Atahan-Evrenk, D. H. Kim, S. Y. Lee, H. A. Becerril, A. Aspuru-Guzik, M. F. Toney, Z. Bao, *Nature* **2011**, *480*, 504.
- [8] K. Zhang, M. Borkowski, P. Wucher, P. M. Beaujuge, J. J. Michels, P. W. M. Blom, T. Marszalek, W. Pisula, *Adv. Electron. Mater.* **2021**, *7*, 2100397.
- [9] S. Wang, M. Kappl, I. Liebewirth, M. Muller, K. Kirchhoff, W. Pisula, K. Müllen, *Adv. Mater.* **2012**, *24*, 417.
- [10] Y. Diao, L. Shaw, Z. Bao, S. C. B. Mannsfeld, *Energy Environ. Sci.* **2014**, *7*, 2145.
- [11] a) R. Z. Rogowski, A. Dzwilewski, M. Kemerink, A. A. Darhuber, *J. Phys. Chem. C* **2011**, *115*, 11758; b) K. Zhang, Z. Wang, T. Marszalek, M. Borkowski, G. Fytas, P. W. M. Blom, W. Pisula, *Mater. Horiz.* **2020**, *7*, 1631.
- [12] a) G. Wypych, in *Kirk-Othmer Encyclopedia of Chemical Technology*, Solvents, Industrial, June **2006**, <https://doi.org/10.1002/0471238961.1915122219211212.a01.pub2>; b) X. Gu, L. Shaw, K. Gu, M. F. Toney, Z. Bao, *Nat. Commun.* **2018**, *9*, 534.
- [13] a) H. A. Becerril, M. E. Roberts, Z. Liu, J. Locklin, Z. Bao, *Adv. Mater.* **2008**, *20*, 2588; b) G. Giri, E. Verploegen, S. C. Mannsfeld, S. Atahan-Evrenk, D. H. Kim, S. Y. Lee, H. A. Becerril, A. Aspuru-Guzik, M. F. Toney, Z. Bao, *Nature* **2011**, *480*, 504.
- [14] a) F. J. Lin, C. Guo, W. T. Chuang, C. L. Wang, Q. Wang, H. Liu, C. S. Hsu, L. Jiang, *Adv. Mater.* **2017**, *29*, 1606987; b) G. Wang, W. Huang, N. D. Eastham, S. Fabiano, E. F. Manley, L. Zeng, B. Wang, X. Zhang, Z. Chen, R. Li, R. P. H. Chang, L. X. Chen, M. J. Bedzyk, F. S. Melkonyan, A. Facchetti, T. J. Marks, *Proc. Natl. Acad. Sci. USA* **2017**, *114*, E10066.
- [15] a) R. L. Headrick, S. Wo, F. Sansoz, J. E. Anthony, *Appl. Phys. Lett.* **2008**, *92*, 063302; b) Y. Li, J. Wan, D. M. Smilgies, N. Bouffard, R. Sun, R. L. Headrick, *Sci. Rep.* **2016**, *6*, 32620.
- [16] a) A. Tracz, T. Makowski, S. Masirek, W. Pisula, Y. H. Geerts, *Nanotechnology* **2007**, *18*, 485303; b) J. Piris, M. G. Debije, N. Stutzmann, B. W. Laursen, W. Pisula, M. D. Watson, T. Bjørnholm, K. Müllen, J. M. Warman, *Adv. Funct. Mater.* **2004**, *14*, 1053.
- [17] X. Gu, L. Shaw, K. Gu, M. F. Toney, Z. Bao, *Nat. Commun.* **2018**, *9*, 534.
- [18] J. J. Michels, K. Zhang, P. Wucher, P. M. Beaujuge, W. Pisula, T. Marszalek, *Nat. Mater.* **2020**, *20*, 68.
- [19] Y. Gao, Z. Liu, D. M. Sun, L. Huang, L. P. Ma, L. C. Yin, T. Ma, Z. Zhang, X. L. Ma, L. M. Peng, H. M. Cheng, W. Ren, *Nat. Commun.* **2015**, *6*, 8569.
- [20] a) Z. Zhang, B. Peng, X. Ji, K. Pei, P. K. L. Chan, *Adv. Funct. Mater.* **2017**, *27*, 1703443; b) R. Janneck, F. Vercesi, P. Heremans, J. Genoe, C. Rolin, *Adv. Mater.* **2016**, *28*, 8007; c) R. Janneck, P. Heremans, J. Genoe, C. Rolin, *Adv. Mater. Interfaces* **2018**, *5*, 1800147; d) M. Li, F. Hinkel, K. Müllen, W. Pisula, *Nanoscale* **2016**, *8*, 9211.
- [21] M. Chen, B. Peng, S. Huang, P. K. L. Chan, *Adv. Funct. Mater.* **2020**, *30*, 1905963.
- [22] R. Janneck, D. Karagiannis, P. Heremans, J. Genoe, C. Rolin, *Adv. Mater. Interfaces* **2019**, *6*, 1900614.
- [23] a) F. Zhang, E. Mohammadi, X. Luo, J. Strzalka, J. Mei, Y. Diao, C. Rolin, *Adv. Mater. Interfaces* **2018**, *5*, 1800147.
- [24] a) Z. Chai, S. A. Abbasi, A. A. Busnaina, *ACS Appl. Mater. Interfaces* **2018**, *10*, 18123; b) S. Riera-Galindo, A. Tamayo, M. Mas-Torrent, *ACS Omega* **2018**, *3*, 2329.
- [25] a) C. R. Derjaguin, *Dokl. Acad. Sci. U.S.S.R.* **1943**, *39*, 13; b) L. L. a. B. Levich, *Acta Physicochim. URSS* **1942**, *17*, 141.
- [26] a) T. Izawa, E. Miyazaki, K. Takimiya, *Adv. Mater.* **2008**, *20*, 3388; b) H. Ebata, T. Izawa, E. Miyazaki, K. Takimiya, M. Ikeda, H. Kuwabara, T. Yui, *J. Am. Chem. Soc.* **2007**, *129*, 15732.
- [27] a) R. Janneck, D. Karagiannis, P. Heremans, J. Genoe, C. Rolin, *Adv. Mater. Interfaces* **2019**, *6*, 1900614; b) B. Peng, Z. Wang, P. K. L. Chan, *J. Mater. Chem. C* **2016**, *4*, 8628.
- [28] a) C. Hsueh, F. Doumenc, B. Guerrier, *Eur. Phys. J.: Spec. Top.* **2013**, *219*, 51; b) K. Zhang, T. Marszalek, P. Wucher, Z. Wang, L. Veith, H. Lu, H. J. Räder, P. M. Beaujuge, P. W. M. Blom, W. Pisula, *Adv. Funct. Mater.* **2018**, *28*, 1805594.
- [29] a) M. L. Berre, Y. Chen, D. Baigl, *Langmuir* **2009**, *25*, 2554; b) F. Doumenc, J. B. Salmon, B. Guerrier, *Langmuir* **2016**, *32*, 13657.
- [30] G. Jing, H. Bodiguel, F. Doumenc, E. Sultan, B. Guerrier, *Langmuir* **2010**, *26*, 2288.
- [31] J.-C. Lee, J.-O. Kim, H.-J. Lee, B. Shin, S. Park, *Chem. Mater.* **2019**, *31*, 7377.
- [32] F. Doumenc, B. Guerrier, *Europhys. Lett.* **2013**, *103*, 14001.
- [33] H. Bodiguel, F. Doumenc, B. Guerrier, *Langmuir* **2010**, *26*, 10758.

- [34] A. Perez-Rodriguez, I. Temino, C. Ocal, M. Mas-Torrent, E. Barrena, *ACS Appl. Mater. Interfaces* **2018**, *10*, 7296.
- [35] a) L. Li, P. Gao, K. C. Schuermann, S. Ostendorf, W. Wang, C. Du, Y. Lei, H. Fuchs, L. De Cola, K. Mullen, L. Chi, *J. Am. Chem. Soc.* **2010**, *132*, 8807; b) Y. Su, X. Gao, J. Liu, R. Xing, Y. Han, *Phys. Chem. Chem. Phys.* **2013**, *15*, 14396.
- [36] M. Habibi, P. Moller, A. Fall, S. Rafai, D. Bonn, *Soft Matter* **2012**, *8*, 4682.
- [37] S. Kwon, J. Kim, G. Kim, K. Yu, Y. R. Jo, B. J. Kim, J. Kim, H. Kang, B. Park, K. Lee, *Adv. Mater.* **2015**, *27*, 6870.
- [38] J. H. Lee, Y. Seo, Y. D. Park, J. E. Anthony, D. H. Kwak, J. A. Lim, S. Ko, H. W. Jang, K. Cho, W. H. Lee, *Sci. Rep.* **2019**, *9*, 21.
- [39] a) K. Zhang, N. B. Kotadiya, X. Y. Wang, G. J. A. H. Wetzelaer, T. Marszalek, W. Pisula, P. W. M. Blom, *Adv. Electron. Mater.* **2020**, *6*, 1901352; b) A. Ablat, A. Kyndiah, G. Houin, T. Y. Alic, L. Hirsch, M. Abbas, *Sci. Rep.* **2019**, *9*, 6685.
- [40] M. Waldrip, O. D. Jurchescu, D. J. Gundlach, E. G. Bittle, *Adv. Funct. Mater.* **2019**, *30*, 1904576.
- [41] T. Shen, H. Zhou, X. Liu, Y. Fan, D. D. Mishra, Q. Fan, Z. Yang, X. Wang, M. Zhang, J. Li, *ACS Omega* **2020**, *5*, 10891.
- [42] H. H. Choi, K. Cho, C. D. Frisbie, H. Sirringhaus, V. Podzorov, *Nat. Mater.* **2018**, *17*, 2.
- [43] W. L. Kalb, B. Batlogg, *Phys. Rev. B* **2010**, *81*, 035327.